POLITECNICO DI TORINO
Repository ISTITUZIONALE

Multimodal surface-wave tomography to obtain S- and P-wave velocities applied to the recordings of unmanned aerial vehicle deployed sensors

Terms of use:

Publisher copyright

(Article begins on next page)

01 May 2024

Multimodal surface-wave tomography to obtain S- and P-wave velocities applied to the recordings of unmanned aerial vehicle deployed sensors

Farbod Khosro Anjom[1], Thomas Jules Browaeys[2], and Laura Valentina Socco[1]

ABSTRACT

Exploration seismic surveys in hard-to-access areas such as foothills and forests are extremely challenging. The Multiphysics Exploration Technologies Integrated System (METIS) research project was initiated to design an exploration system, facilitating the acquisition in these areas by delivering the receivers from the sky using unmanned aerial vehicles. Air dropping of the sensors in vegetated areas results in an irregular geometry for the acquisition. This irregularity can limit the application of conventional surface wave methods. We have developed a surface wave workflow for estimating the S-wave velocity (V_S) and P-wave velocity (V_P) models and that supports the irregular geometry of the deployed sources and receivers. The method consists of a multimodal surface-wave tomography (SWT) technique to compute the V_S model and a data transform method (the wavelength/depth [W/D] method) to determine the Poisson's ratio and V_P model. We applied the method to the METIS's first pilot records, which were acquired in the forest of Papua New Guinea. Application of SWT to the data resulted in the first 90 m of the V_S model. The W/D method provided the Poisson's ratio averaged over the area and the V_P model between 10 and 70 m from the surface. The impact of the acquisition scale and layout on the resolution of the estimated model and the advantages of including the higher modes of surface waves in the tomographic inversion are assessed in detail. The presence of shots from diverse site locations significantly improves the resolution of the obtained model. Including the higher modes enhances the data coverage and increases the investigation depth.

INTRODUCTION

A significant fraction of onshore oil and gas deposits is in remote areas with limited access, extreme environments, and challenging topography, such as foothills, forests, and deserts. The difficulty in transporting and deploying the acquisition equipment, as well as the natural hazards associated with these unmarked regions, makes the seismic acquisition very challenging. The conventional seismic-data acquisition method in these areas usually leads to cost overruns, delays, and a significant environmental footprint. In the age of technological developments and innovations, the Multiphysics Exploration Technologies Integrated System (METIS) research project was created to reform the conventional acquisition methods and enable seismic imaging of these areas (Lys et al., 2018). In the scheme of METIS, the sensors are placed in the 40 cm downfall air receiver technology (DARTs), and drones are used to deliver and

drop them to predefined positions. The DARTs are equipped with radio transmitters that enable real-time recording (Pagliccia et al., 2018).

The first METIS pilot was performed in the foothills of Papua New Guinea (PNG) forests. The violent rains, intense humidity, high temperatures, and dense vegetation make the foothills of PNG an extreme environment for acquiring seismic data. The PNG data acquisition was a success and satisfied the objectives of METIS (Lys et al., 2018). Here, we use these data to obtain near-surface S-wave velocity (V_S) and P-wave velocity (V_P) models by analyzing the surface waves.

Surface waves (groundroll) contain important information regarding the shallow subsurface and are usually dominant in the recordings (Socco et al., 2010). As a result, they are good candidates for near-surface characterization. The phase velocities of the surface wave propagation in layered media are characterized by geometric

[1]Politecnico di Torino, DIATI, 24, Duca degli Abruzzi Street, 10141 Turin, Italy. E-mail: khosro-anjom.farbod@polito.it (corresponding author); valentina.socco@polito.it.
[2]Total EP, Avenue Larribau, 64000 Pau, France. E-mail: jules.browaeys@total.com.

dispersion. The so-called surface-wave dispersion curves (DCs, phase velocity versus frequency) are estimated and inverted to reconstruct the near-surface model. The most common surface wave analysis method is based on multichannel recordings from an array of receivers, which are used to compute a DC through wavefield transform. Then, the DC is inverted to estimate a 1D V_S model assigned to the center of the receiver array. Despite many efforts to enhance the lateral resolution of the estimated DCs, the multichannel method still suffers from low lateral resolution (Mi et al., 2017). Moreover, many multichannel methods require 2D geometries and/or evenly spaced receivers (e.g., the *f-k* method using the regular Fourier transform). In the scheme of METIS, the deployment geometry of the sources and receivers is based on the so-called carpet recording, in which a fine grid of receivers is deployed, and the number of sources is limited only to the accessible locations (Lys et al., 2018). In the PNG pilot, the geometry of the deployed receivers was also affected by the forest vegetation: The receivers were delivered only into the spaces between trees. The limited sky access resulted in an irregular layout of the receiver spread. The surface wave multichannel approach can still be applied to these data by selecting multiple receiver spreads over a 3D area. However, this could lead to erroneous estimated DCs and failure in retrieving the lateral variations in the inversion step.

An alternative approach in this kind of acquisition framework is surface-wave tomography (SWT), which supports the irregular acquisition layout and results in high-resolution model estimation. SWT is a well-established method in earthquake seismology for V_S reconstruction of the crust and upper mantle (e.g., Shapiro et al., 2005; Yao et al., 2006; Boiero, 2009; Bao et al., 2015; Wespestad et al., 2019). Recently, a few authors showed the SWT applications for the near-surface characterization using active (e.g., Socco et al., 2014; Da Col et al., 2019) and passive data (Picozzi et al., 2009; Badal et al., 2013).

Surface wave propagation is a multimodal phenomenon. Although, usually, the fundamental mode of the surface wave is solely excited or dominant in the whole bandwidth, under certain conditions of the site and the source, multiple modes of surface waves can be created. When available, higher mode data should be included in the inversion because they represent additional information that can improve the model parameter resolution and also increase the investigation depth thanks to the different displacement patterns of higher modes (Ganji et al., 1998). The PNG data set is characterized by the multimodal propagation of the surface waves. In SWT methods, the recordings of a receiver pair aligned with a source are used to estimate multiple path-averaged DCs. Unlike the multichannel method, the two-station method does not provide enough resolution to estimate multiple surface-wave modes. We propose a two-station method that includes the muting in the *x-t* domain and enables the estimation of multiple modes of surface waves. The proposed method focuses on estimating a specific surface wave mode at each attempt, in which a proper mute based on the preliminary multichannel analysis of the data is used to damp the other modes.

Most surface wave methods focus on estimating the V_S model only, and they require a priori V_P and Poisson's ratio for the inversion step (Socco et al., 2010). Few researchers have investigated the possibility of estimating V_P from surface waves (Xia et al., 2003; Bergamo and Socco, 2016; Socco and Comina, 2017). Socco et al. (2017) discover a strong correlation between DC and the time-average V_S (VSZ) that can be directly used to compute the static corrections. They show that there exists a relationship between the wavelength of DCs and the skin depth of surface waves (the wavelength-depth [W/D] relationship). To construct the W/D relationship, a reference DC and the corresponding VSZ model is required. The W/D relationship represents the wavelength and depth couples corresponding to the equal surface wave phase velocity and VSZ. Socco and Comina (2017) prove that the W/D relationship is highly sensitive to Poisson's ratio. They develop a method to estimate time-average V_P (VPZ), exploiting only the W/D relationship. Khosro Anjom et al. (2019) show that, by using a Dix-type equation and by imposing total variation regularization, it is possible to transform VSZ and VPZ into interval V_S and V_P. The interval V_S and V_P velocities can be used to estimate the Poisson's ratio.

The purpose of this paper is to provide a multimodal SWT workflow that supports METIS's acquisition outline and provides V_S and V_P model estimates. The proposed multimodal SWT method consists of a two-station method to estimate the path-averaged DCs and a tomographic inversion (Boiero, 2009) to estimate the V_S model. To obtain the a priori Poisson's ratio required for the tomographic inversion and determine the V_P model, we use the multichannel analysis and the W/D method (Socco and Comina, 2017; Socco et al., 2017; Khosro Anjom et al., 2019). Here, we show and evaluate the application of the method to the PNG data set.

PNG DATA FROM THE METIS PILOT STUDY

The PNG pilot study was performed in December 2017 over an area of approximately 0.2 km². Before the acquisition, 25 holes (approximately 2 m) were dug for mud-gun sources. In addition, the location and the size of the gaps between the trees (sky holes) were identified using an airborne lidar survey. The sky holes are the locations where the DARTs are expected to land safely. The prototype DARTs were equipped with 10 Hz geophones and weighted approximately 1 kg. The drone could carry four DARTs at a time. Figure 1a and 1b shows the prototype drone and DART, whereas Figure 1c presents a real view of a drone dropping a DART in a sky hole.

The mud guns were pressurized to 13.8 MPa to generate the airflow, and the real-time vertical displacement velocity was recorded at 4 ms sampling rate and for a time window of 6.0 s. A total of 81 deployed DARTs properly landed on the ground with good
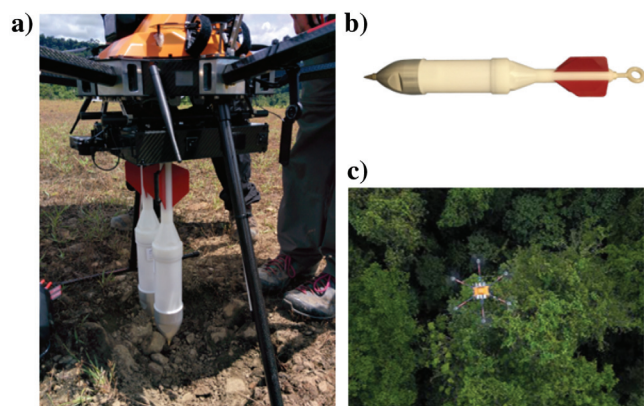

Figure 1. (a) The drone used in the PNG data acquisition, (b) a DART, and (c) real view of a drone dropping a DART into a sky hole (Pagliccia et al., 2018).

coupling. However, the data from 43 geophones were not recovered due to the difficulties of wireless transmission through the jungle vegetations toward a single collecting antenna. At the end of the pilot acquisition, the seismic crew collected the geophones, thanks to the sensors' positions registered by the global positioning system. Currently, the METIS team is working on biodegradable sensors to eliminate the need for sensor recovery after the acquisition.

In Figure 2a, we show the deployment geometry of the receivers and the shots. At each source's location, between five to eight shots were performed. We removed the saturated signals before the stacking of the traces.

In Figure 2b, we show the first 3 s of the normalized recordings from the shot location highlighted in Figure 2a. The records are displayed on a spatial axis that represents the source-receiver offset. The first breaks are available for all receivers, although they are less evident at the far offset. In Figure 2b, the solid red lines show the surface wave's time panel boundaries. The data show the excitation of the fundamental mode and the first higher mode of the surface wave; the separation of the two surface wave modes is evident in the offset beyond 300 m. The two surface wave modes can also be observed in the frequency-velocity spectrum in Figure 2c. The estimated fundamental mode and the first higher mode are very well separated in the whole frequency band and are shown in blue and red, respectively. In Figure 2c, the spectrum of the records shows that surface wave energy exists between 5 and 20 Hz. However, depending on the source-receiver offset, the surface wave is present up to 55 Hz. As a result, we estimate the path-averaged DCs required for the SWT within a 5–55 Hz frequency band.

PROCESSING WORKFLOW

The detailed steps of the multimodal SWT workflow applied to the PNG data set are given in the schematic diagram in Figure 3. The workflow's final task is to obtain a 3D V_S and V_P model of the subsurface over the area covered by the receivers. The workflow is divided into two main parts: multistation DC analysis and SWT. The first is a preliminary analysis to define the trend of the dispersion over the whole area and use it as a guide during SWT processing. Moreover, the multichannel DCs will be used to obtain a velocity limit separating different modes of the surface waves and to estimate Poisson's ratio. The second part aims to estimate the path-averaged DCs along the path of a high number of receiver pairs and invert them for a high-resolution 3D V_S model that will be further converted into V_P thanks to the Poisson's ratio estimated in the first part. In Figure 3, the green and red rectangles highlight the multichannel analysis and the SWT processing, respectively.

The data set suggested excitation of the fundamental and first higher mode of the surface waves. As a result, we prepared the workflow for these two modes; however, a similar method can be applied when various surface-wave modes are ex-
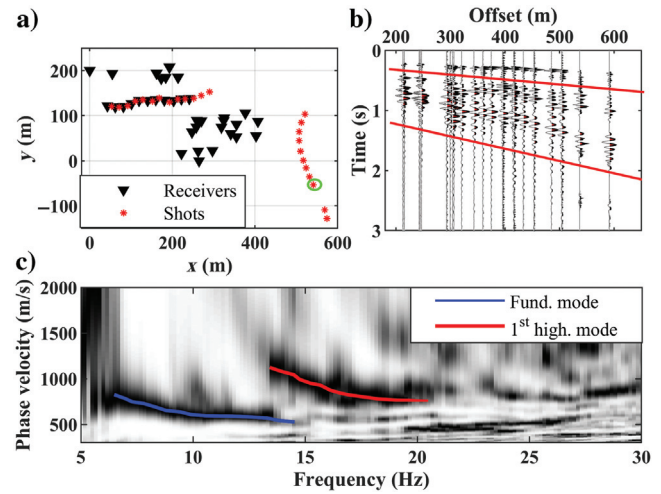

Figure 2. (a) The outline of PNG acquisition used for SWT. (b) The recordings from the highlighted (the green circle) shot in (a). (c) The frequency-velocity spectrum, corresponding to the seismic data in (b).
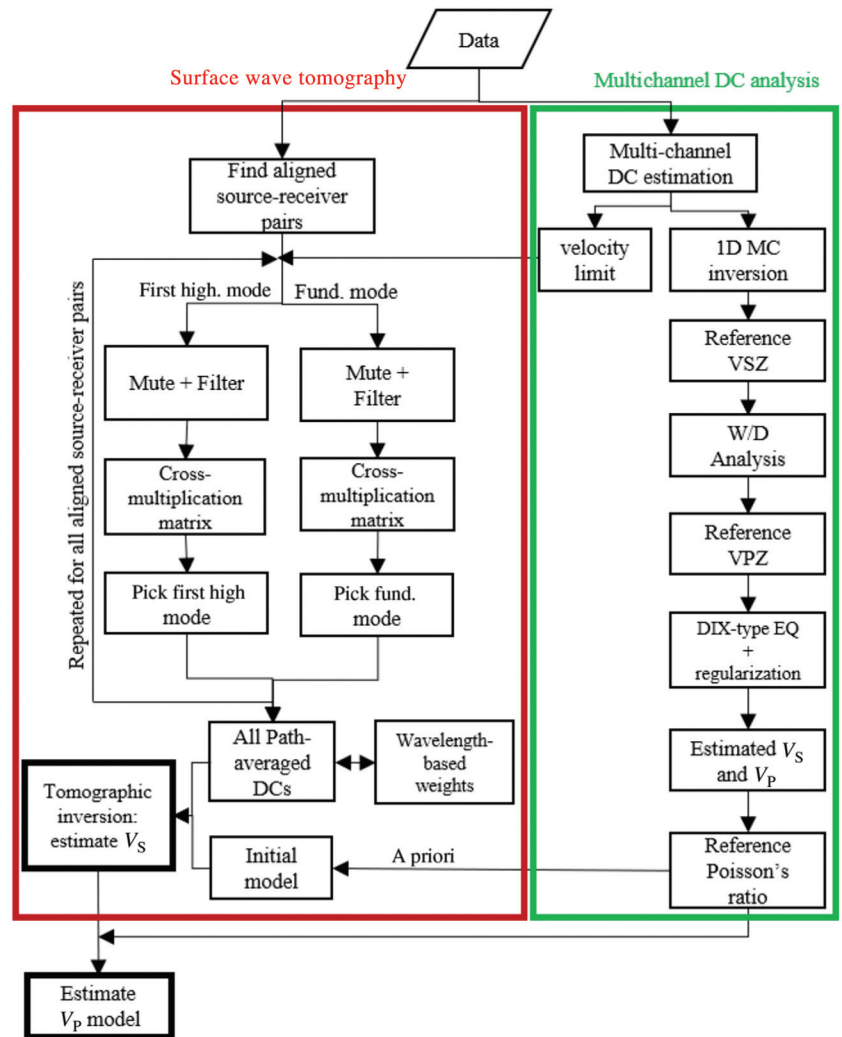

Figure 3. The full SWT workflow used to estimate the V_S and V_P models, in which the steps are divided into multichannel DC analysis in green and SWT in red.

cited. The condition for the feasibility of this strategy is that the modes are clearly separated in the whole processed frequency band.

Multichannel DC analysis of surface waves

In this part of the analysis, we make strong simplifying assumptions. We select subsets of receivers, and we neglect the underlying
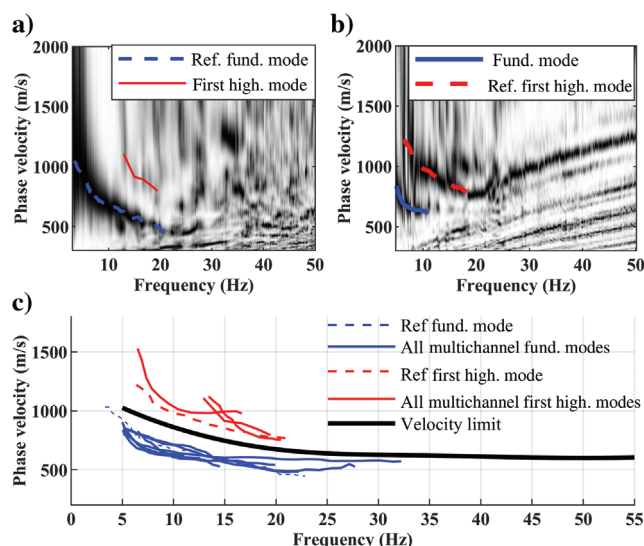

Figure 4. Multichannel analysis of the data set. (a) The spectrum used to compute the reference fundamental mode. (b) The spectrum used to compute the reference first higher mode. (c) All estimated fundamental modes (in blue) and first higher modes (in red) using the multichannel method and the velocity limit (in black).
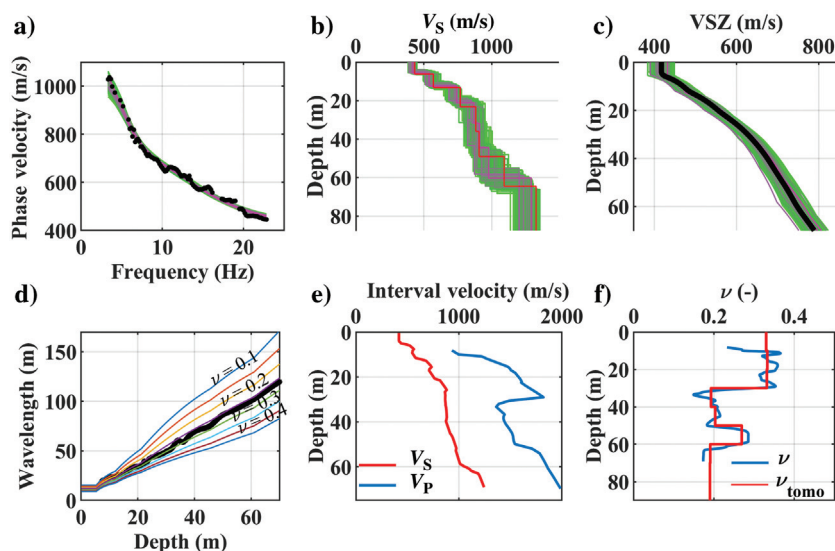

Figure 5. The W/D method to obtain the reference Poisson's ratio. (a) The reference fundamental mode with the DCs of the accepted models. (b) The V_S of the accepted models. (c) The VSZ of the accepted models, in which the reference VSZ is shown in black. (d) The estimated W/D relationship shown with the synthetic W/D relationships, each with a constant Poisson's ratio. (e) The computed V_S and V_P models corresponding to the reference fundamental mode. (f) The estimated Poisson's ratio corresponding to the reference fundamental mode in blue and the adopted Poisson's ratio for the tomographic inversion in red.

lateral subsurface heterogeneity. Hence, we extract the relevant DC, considering only the offset from the source and neglecting that the receivers are spatially distributed and have different azimuth with respect to the source point. We also stack the contribution of different sources, thus averaging over the whole azimuth range. We use the multichannel phase-shift method (Park et al., 1998), with which it is possible to compute the frequency-velocity spectrum corresponding to receiver spreads with irregular spacing and separate the different surface wave modes.

We estimated DCs using various sets of sources and receivers of the data set. In Figure 4a and 4b, we show the frequency-velocity spectrum corresponding to two different sources and receiver deployment geometry. The estimated fundamental mode and the first higher mode are shown in blue and red, respectively.

Figure 4c shows all estimated fundamental and first higher modes of surface waves using multichannel analysis. We used these DCs to manually design a velocity limit that separates the fundamental and first higher modes of the data. In Figure 4c, we also show the adopted velocity limit in black. We will use the velocity limit in the SWT processing step to separate the different modes of surface waves. Because the modal curves are only used to define the limit between the fundamental and first higher modes, we estimated as many curves as possible, also picking weak spectral maxima, such as the estimated first higher mode in Figure 4a. Among the estimated DCs, we selected the reference fundamental and first higher modes based on the frequency band. For the reference fundamental mode, we considered the broadband DC that includes the low-frequency elements. Figure 4c also shows the reference fundamental and first higher modes with the dashed blue and red lines, respectively. The reference modal curves are used to find the correct trend of the two-station DCs. We also perform the W/D method on the reference fundamental mode to estimate a priori Poisson's ratio required for the SWT.

Poisson's ratio: The W/D method

To compute a priori Poisson's ratio required for the tomographic inversion, we use the W/D data transform workflow proposed by Khosro Anjom et al. (2019). We assume negligible lateral variations of Poisson's ratio, and we use the reference fundamental mode from the multichannel analysis to compute an average 1D Poisson's ratio corresponding to the investigation area.

Figure 5 presents the W/D method's steps applied to the reference fundamental mode (Figure 4a). Considering a variable Poisson's ratio in a wide range (0.1–0.45), we inverted the reference fundamental mode using a Monte Carlo inversion (Socco and Boiero, 2008). We used the statistical Fisher test with a low level of confidence (0.05) to select all models that belong to the best-fitting model population. In Figure 5a and 5b, we show the selected DCs and the corresponding V_S models. The V_S of the accepted models was transformed into VSZ using a reverse Dix-type equation (Socco et al., 2017). The accepted VSZ models were averaged at each depth to estimate a reference VSZ model corresponding to the reference fundamental mode. In Figure 5c,

we show the accepted and the reference VSZ models. The estimated VSZ and the reference DC were used to compute the experimental W/D relationship (Figure 5d). We then used the W/D relationship's sensitivity to Poisson's ratio (Socco and Comina, 2017) to estimate the apparent Poisson's ratio and the reference VPZ model. Then, we used a Dix-type equation and imposed total variation regularization (Khosro Anjom et al., 2019) to transform the VSZ and VPZ into interval V_S and V_P (Figure 5e). Finally, having estimated the V_S and the V_P models, we computed the 1D Poisson's ratio (Figure 5f) corresponding to the reference fundamental mode.

Path-averaged DCs estimation using the two-station method

The first step of the SWT is to estimate the path-averaged DCs. These DCs are estimated using the recordings from receiver couples aligned with a source. We implement an automatic algorithm to find the receiver couples aligned with the source at each azimuth angle, considering 1° tolerance for the deviation from a linear path. We filter the receiver couples' traces to center frequencies within the required band, using zero-phase Gaussian filters. Then, the filtered traces of the receiver couples are crosscorrelated and assembled to form the cross-multiplication matrix. We use a third-order spline interpolator to convert the cross-multiplication matrix to the frequency-velocity domain. Finally, at each frequency, the phase velocity is picked as the maximum of the cross-multiplication matrix, closest to the reference DC.

Unlike multistation methods, the two-station method does not deliver enough resolution to detect and pick multiple modes of surface waves. As a result, in the presence of multiple modes (such as the PNG data set), it is imperative to isolate each mode before performing the crosscorrelation of the recordings (Halliday and Curtis, 2008). Yao et al. (2006) compute each recording's group velocity, and they use it to window the traces before applying the two-station method. This method amplifies the fundamental mode and dampens the other events available in the recordings; however, picking the group velocity of all traces is very time-consuming. Besides, using the higher modes in the process instead of losing them can improve the investigation depth and enhance the resolution of the final V_S model (Ganji et al., 1998; Xia et al., 2003). We propose a muting technique based on which a dispersive velocity limit is used to automatically mute the seismic data and isolate multiple modes of the surface waves. We use the multichannel DCs to identify the velocity limit that best separates the fundamental and first higher modes. We mute the recordings before applying the two-station method and perform the two-station method separately for the computation of each mode of surface waves. Depending on whether the fundamental mode or the first higher mode is needed to be isolated, we apply the velocity limit as a half-Gaussian mute to the relevant time panel of the pair receivers' recordings. Appendix A presents detailed steps of the two-station method.

In total, 505 possible paths were identified for the data set. We used the velocity limit obtained in Figure 4c to isolate the fundamental and first higher modes of the surface wave. In Figure 6,

we show an example of two-station method applied to the recordings of a receiver pair for picking the fundamental mode (Figure 6a and 6b) and first higher mode (Figure 6c and 6d), respectively. We only picked the data points relevant to wavelengths smaller than twice the distance between the receiver pair (the half-wavelength rule; Heisey et al., 1982; Nazarian et al., 1983; Yao et al., 2006). In Figure 6a and 6c, we show the half-wavelength line in white. We also show the reference fundamental and first higher modes obtained from multichannel analysis; we used the reference DCs to locate the right trend when picking the two-station DCs.
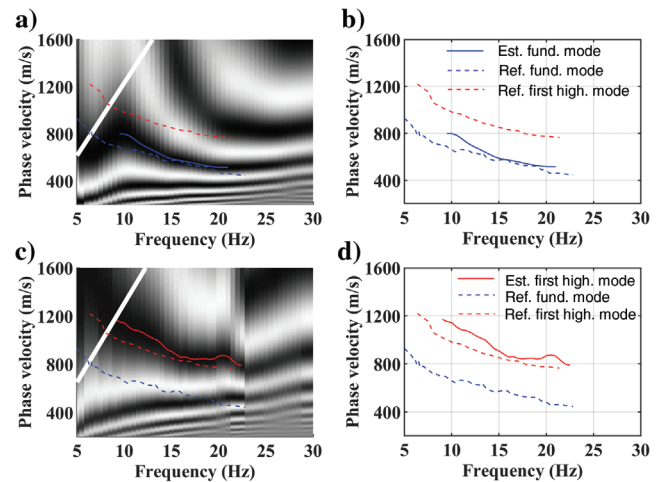

Figure 6. Example two-station pickings from the data set, in which the dashed lines are the reference DCs. (a) The fundamental mode cross-multiplication matrix, in which the white line is the half-wavelength limit. (b) The estimated fundamental mode from the cross-multiplication matrix in (a). (c) The first higher mode cross-multiplication matrix, in which the white line is the half-wavelength limit. (d) The estimated first higher mode from the cross-multiplication matrix in (c).
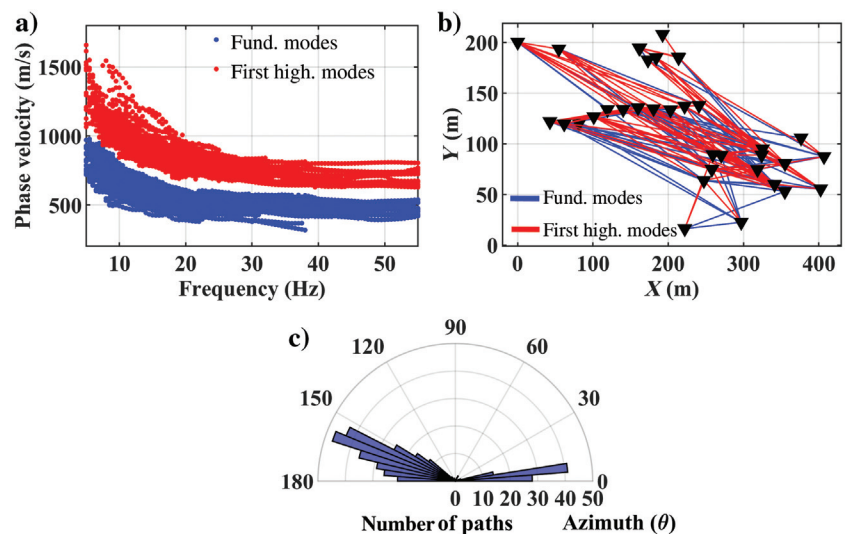

Figure 7. (a) The estimated DCs, (b) the observed paths, and (c) the azimuthal illumination, in which the numbers around the greatest circle are the azimuths and the smaller circles show the number of available paths.
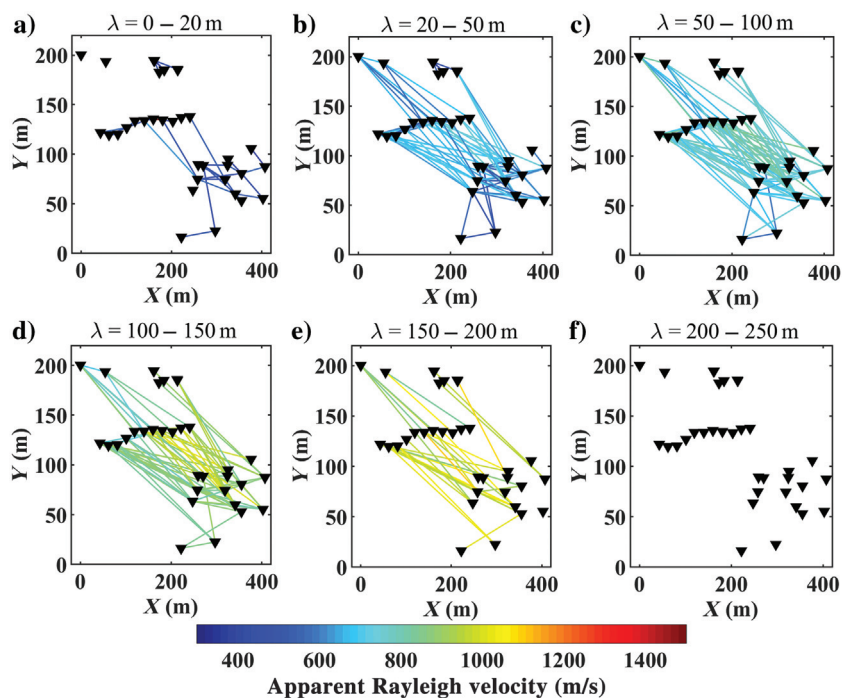
Figure 8. The data coverage of the estimated surface wave fundamental modes as pseudoslices corresponding to different wavelength intervals: (a) between 0 and 20 m, (b) between 20 and 50 m, (c) between 50 and 100 m, (d) between 100 and 150 m, (e) between 150 and 200 m, and (f) between 200 and 300 m.
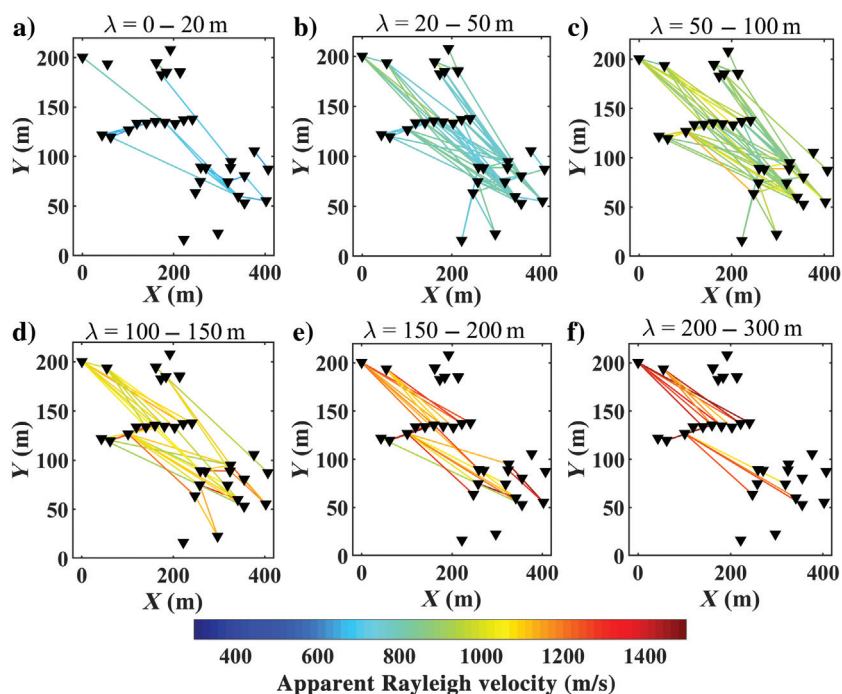

Figure 9. The data coverage of the estimated surface wave first higher modes as pseudoslices corresponding to different wavelength intervals: (a) between 0 and 20 m, (b) between 20 and 50 m, (c) between 50 and 100 m, (d) between 100 and 150 m, (e) between 150 and 200 m, and (f) between 200 and 300 m.

In total, we computed 198 fundamental modes and 168 first higher modes. The remaining paths presented a noisy cross-multiplication matrix, and they were discarded from the data. In Figure 7a and 7b, we show all of the estimated DCs and the corresponding data coverage (paths). In Figure 7c, we show the azimuthal illumination of the estimated DCs as a polar plot; most of the paths have azimuth angles between 0°–25° and 150°–179°.

The resolution and investigation depth of the inversion is directly related to the wavelength coverage of the estimated DCs. The wavelength coverage for 3D data can be evaluated as pseudoslices (Da Col et al., 2019), in which, for a wavelength range, the available paths are plotted with a color corresponding to the average phase velocity (the apparent phase velocity). Figure 8a–8f shows the fundamental modes' pseudoslices corresponding to six wavelength ranges.

The pseudoslices are useful tools for locating possible lateral variations or outliers that do not corroborate with the apparent phase velocity of similar paths; for example, in Figure 8d, a significant velocity contrast is observed, indicating a considerable lateral variation. Figure 8a shows inadequate coverage for the wavelength range of 0–20 m; thus, a low resolution should be expected in recovering the first few meters of the model. The wavelength coverage shows the highest number of paths between 20 and 150 m (Figure 8b–8d), whereas the coverage vanishes for the wavelengths greater than 200 m (Figure 8f).

In Figure 9a–9f, we show the pseudoslices corresponding to the first higher modes within the same six wavelength ranges as we used for the fundamental mode (Figure 8). Similar to fundamental modes, for the wavelength range between 0 and 20 m, the wavelength coverage for the first higher mode is limited to a few paths (Figure 9a). The coverage reaches its maximum between 20 and 100 m of wavelength (Figure 9b–9c), and it declines afterward. Unlike fundamental modes (Figure 8f), the first higher mode shows coverage up to 300 m of wavelength (Figure 9f).

Tomographic inversion

The tomographic inversion is based on Boiero (2009). Concerning the formulation of Boiero (2009), we included higher modes, and we introduced a weighting system based on the wavelength of the DC data.

Model

The inputs of the inversion are the estimated path-averaged DCs and the reference (initial) model. The model is a regular grid of laterally invariant 1D models (model points). The param-

eters of the model are the thickness, V_S, Poisson's ratio, and density. The only parameter that updates in the inversion is V_S, whereas the others are fixed a priori; thus, the number of unknowns of the inversion is the number of the model points multiplied by the number of the layers plus one (the half-space). We use constant thicknesses for the layers within the investigation depth. We define the initial V_S model based on the trend of the selected V_S models from the Monte Carlo inversion of the reference fundamental mode obtained through multichannel processing. Considering negligible lateral variations for the Poisson's ratio, we use the reference Poisson's ratio from the W/D method as the prior information for the SWT inversion. Although the inversion is not very sensitive to Poisson's ratio, the a priori Poisson's ratio helps the inversion process to get a more consistent and accurate V_S model. The density has a minor effect on the inversion, and it is chosen based on the information available for the site's geological properties.

We defined the 3D model consisting of 152 laterally invariant 1D models. Each 1D model included nine layers overlying the half-space with a constant thickness of 10 m. The initial model corresponds to 1520 V_S unknowns. The initial V_S model was selected based on the trend of the Monte Carlo inversion of the reference fundamental mode (Figure 5b). The W/D method provided the Poisson's ratio for every 10 cm depth interval between 10 and 70 m from the surface. The values were averaged within 10 m intervals to obtain Poisson's ratio corresponding to each model layer. We extrapolated the Poisson's ratio to cover the full 90 m required for the inversion. In Figure 5f, we show the adopted Poisson's ratio for the tomographic inversion in red. The geologic properties of the very shallow subsurface of a forest suggest very loose and unconsolidated soil. As a result, we considered a low density of 1400 kg/m^3 for the model's first layer. The density of the rest of the layers and the half-space was set at 1800 kg/m^3.

To better comprehend the portion of the data affecting each model point, we computed the number of DC paths crossing each model point, disregarding the wavelength range of the DCs. In Figure 10, we show the obtained data coverage, where the white stands for the zero path crossing the model points. The maximum data coverage is obtained in the center of the model. Except for in the northwest, the data coverage on the model's edges is minimal, suggesting a lower resolution in recovering the V_S of these model points.

Forward operator

In this stage, the synthetic path-averaged DCs corresponding to the observed paths are computed. As the first step, we compute the local 1D synthetic DCs at each model point, using a Haskell (1953) and Thomson (1950) forward model, developed by Maraschini (2008) in MATLAB. Then, we discretize each path to evenly spaced points. For each point and at each frequency, we compute the reciprocal of the phase velocity (slowness) as the bilinear interpolation between the slowness of the four adjacent model points. We then compute the path-averaged synthetic slowness as the mean slowness of all discretized points along the path.

Inversion scheme

The estimated DCs are transformed to slowness and assembled in a single vector as

$$\mathbf{p_{obs}} = [\mathbf{p_{fund.}}; \mathbf{p_{high.}}], \tag{1}$$

where $\mathbf{p_{fund.}}$ and $\mathbf{p_{high.}}$ are the estimated fundamental and first higher modes, respectively. The penetration depth of the surface waves is directly related to the wavelength. The nonuniform sampling of the DC data in terms of wavelength usually drives the inversion algorithms to the shallowest parts of the subsurface (Khosro Anjom and Socco, 2019). We associate a wavelength-based weight to each DC data point, correcting this nonuniformity in depth. For the jth DC, we compute the weights of the ith data point as

$$w_{i,j} = \frac{\Delta\lambda_{i,j}}{\Delta\lambda_{j,\mathrm{max}}}, \tag{2}$$

where $\Delta\lambda_{i,j}$ is the wavelength distance from the closest data point to the data point i. The larger the wavelength distance of the data points, the larger the weight will be. The weights of each DC are normalized to the maximum registered weight $\Delta\lambda_{j,\mathrm{max}}$. For each DC's computation, if many shots from different source locations are stacked, the individual shots can be used to compute a standard deviation for each data point. The obtained uncertainties are used in the inversion to build the covariance matrix corresponding to the data points $\mathbf{p_{obs}}$ as the diagonal matrix:

$$\mathbf{C_{obs}} = \begin{bmatrix} \frac{\sigma_{1,1}^2}{w_{1,1}} & 0 & 0 & 0 & \cdots & 0 \\ 0 & \frac{\sigma_{2,1}^2}{w_{2,1}} & 0 & 0 & \cdots & 0 \\ 0 & 0 & \ddots & 0 & \cdots & 0 \\ 0 & 0 & 0 & \frac{\sigma_{1,2}^2}{w_{1,2}} & \cdots & 0 \\ \vdots & \vdots & \vdots & \vdots & \ddots & \vdots \\ 0 & 0 & 0 & 0 & 0 & \frac{\sigma_{i,j}^2}{w_{i,j}} \end{bmatrix}, \tag{3}$$

where $\sigma_{i,j}$ and $w_{i,j}$ are the standard deviation and the normalized wavelength-based weight of the ith data point of the jth DC, respectively. In Appendix B, we use a synthetic model to show the effect of imposing the wavelength-based weights and including the first higher mode on the tomographic inversion.

We use a weighted least-squares method to invert the estimated DCs, which involves minimizing the misfit function Q:

$$Q = [(\mathbf{p_{obs}} - \mathbf{p(m)})^\mathbf{T} \mathbf{C_{obs}^{-1}} (\mathbf{p_{obs}} - \mathbf{p(m)})]$$
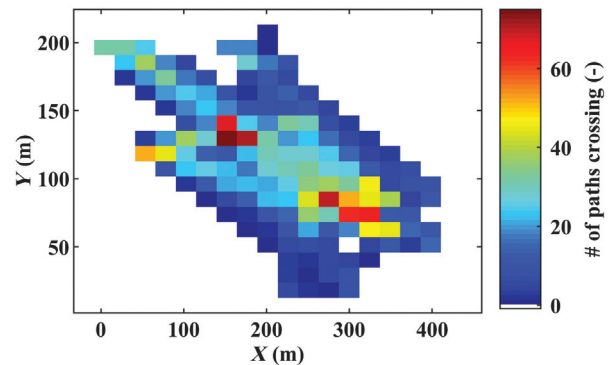$$+ [(-\mathbf{R_p m})^\mathbf{T} \mathbf{C_{Rp}^{-1}} (-\mathbf{R_p m})], \tag{4}$$

Figure 10. The data coverage on the model.

Figure 11. The estimated V_S model for the nine layers corresponding to 90 m of investigation depth: (a) 0–10 m, (b) 10–20 m, (c) 20–30 m, (d) 30–40 m, (e) 40–50 m, (f) 50–60 m, (g) 60–70 m, (h) 70–80 m, and (i) 80–90 m.
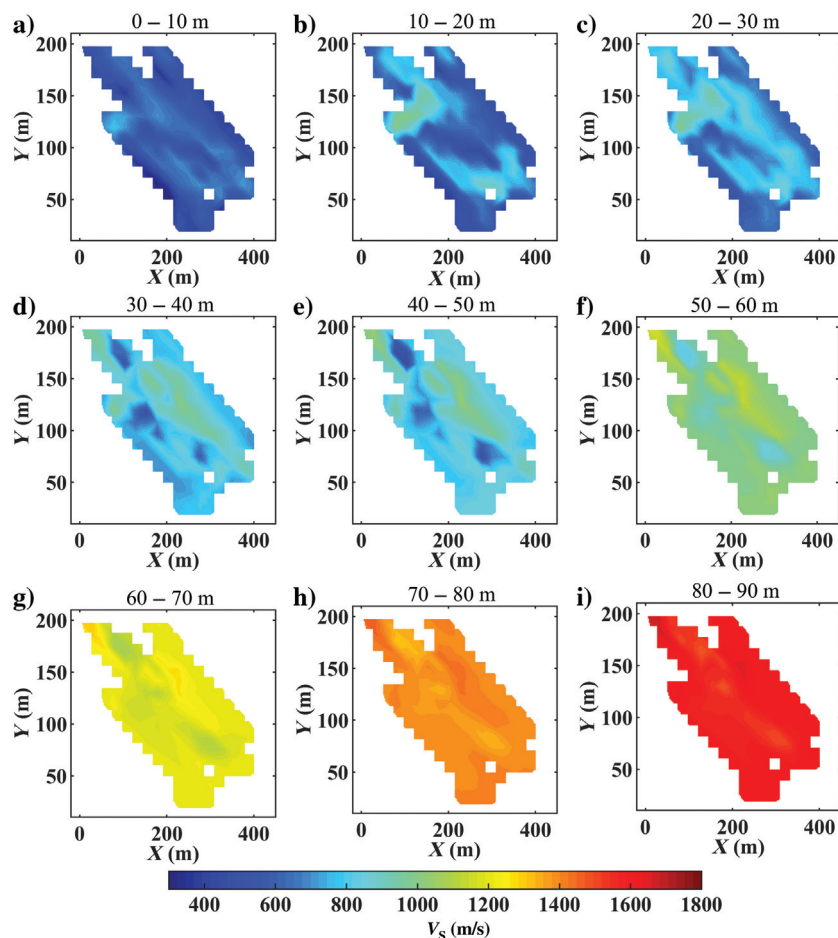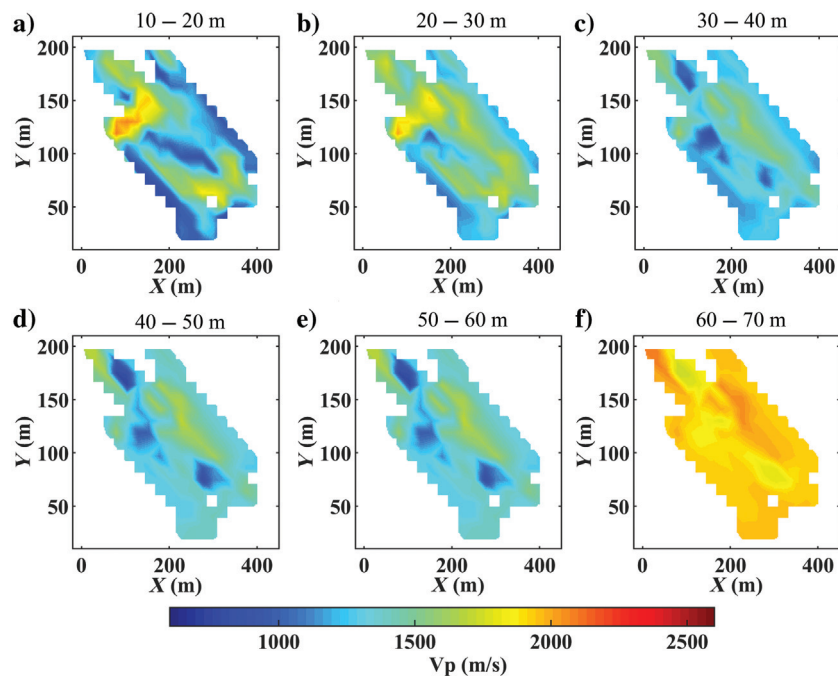
Figure 12. The estimated V_P model between 10 and 70 m using the estimated V_S model in Figure 11 and the reference Poisson's ratio in Figure 5f. (a) 10–20 m, (b) 20–30 m, (c) 30–40 m, (d) 40–50 m, (e) 50–60 m, and (f) 60–70 m.

where the first term is related to the data misfit and the second term is the spatial regularization. The lateral regularization helps with obtaining consistent results (Auken and Christiansen, 2004; Boiero, 2009), and it is achieved by imposing constraints on the variations between the V_S of the adjacent 1D models (Boiero, 2009). The term $\mathbf{R_p}$ is the spatial regularization matrix, which relates the model parameters of the adjacent model points, and $\mathbf{C_{Rp}}$ is the regularization covariance matrix, which defines the strength of the spatial constraints. The term $\mathbf{m}$ is the vector of the model parameters; $\mathbf{p(m)}$ is the vector of the synthetic path-averaged DCs, corresponding to the experimental data points $\mathbf{p_{obs}}$; and $\mathbf{C_{obs}^{-1}}$ is the reciprocal of the covariance matrix shown in equation 3. Similar to Boiero (2009), we use the weighted damped least-squares method (Marquart, 1963) to update the model as

$$
\begin{aligned}
\mathbf{m_{n+1}} = \mathbf{m_n} + &([\mathbf{G^T C_{obs}^{-1} G + R_p^T C_{Rp}^{-1} R_p + \lambda I}]^{-1} \\
&\times [\mathbf{G^T C_{obs}^{-1}(p_{obs} - p(m)) + R_p^T C_{Rp}^{-1}(-R_p m_n)}]), \quad (5)
\end{aligned}
$$

where $\mathbf{G}$ is the Jacobian matrix, which evaluates the sensitivity of the DCs to the model parameters. The terms $\mathbf{m_n}$ and $\mathbf{m_{n+1}}$ are the previous and updated model vectors, respectively.

There were a limited number of shots available for the data set, preventing the computation of the uncertainty for the data points. As a result, we fixed the standard deviation of the data points to 10% of the corresponding phase velocities. We used lateral constraints of 100 m/s to increase the stability of the inversion. The inversion stopped automatically at iteration 49, reaching the misfit minimum.

RESULTS

Figure 11 shows the horizontal slices of the estimated V_S model corresponding to the different layers. In Figure 11d–11g, the estimated V_S model shows a velocity contrast between the east and the west.

We used the reference Poisson's ratio (the blue curve in Figure 5f) to transform the estimated V_S model into the V_P model. In Figure 12, we show the estimated V_P model. The estimated V_P's depth range
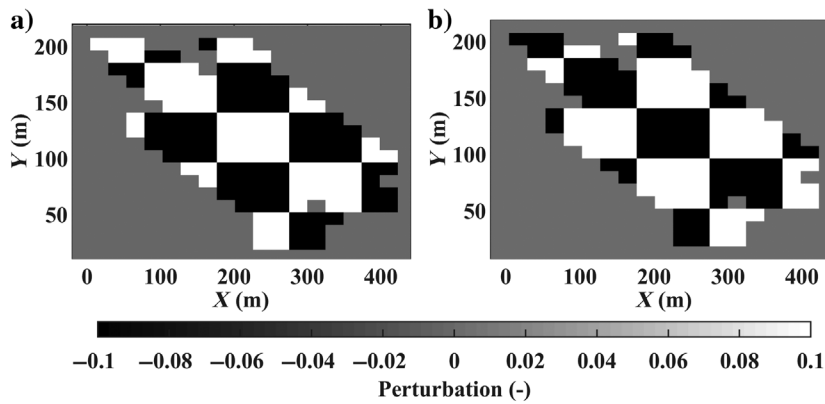

Figure 13. The checkerboard test's perturbation patterns. (a) The pattern used to perturb the model between a depth of 0–40 and 80–90 m. (b) The pattern used to perturb the model at a depth of 40–80 m.
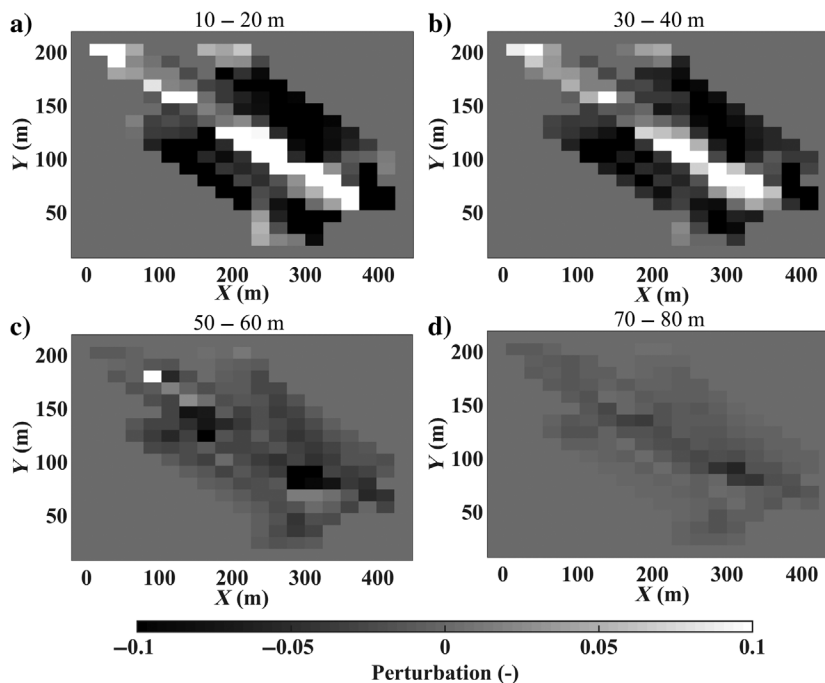

Figure 14. Horizontal sections of recovered perturbations at different layers: (a) 10–20 m, (b) 30–40 m, (c) 50–60 m, and (d) 70–80 m.

depends on the estimated V_S from SWT and the reference Poisson's ratio from the W/D method. The estimated Poisson's ratio is available in a shorter depth range (10–70 m) compared to the estimated V_S (0–90 m). As a result, the estimated V_P in Figure 12 is limited to a depth of 10–70 m. The V_P shows a high velocity between 10 and 30 m of the subsurface. Then, following the drop in Poisson's ratio (Figure 5f), the V_P decreases (Figure 12c). Afterward, the V_P gradually increases until it reaches the maximum velocity (Figure 12f). We estimated a single reference Poisson's ratio averaged over the area, neglecting lateral variations. As a result, the lateral variations of the estimated V_P are solely related to the estimated V_S.

We performed the checkerboard test to assess the spatial resolution of the final model. We perturbed the estimated V_S model (Figure 11) 10%, negatively and positively. In Figure 13a and 13b, we show the horizontal sections of the perturbations. The pattern of the perturbation alternated every 40 m. Therefore, the first 40 m and the last 10 m (80–90 m) of the model were perturbed using the pattern in Figure 13a; the portion of the model between 40 and 80 m of depth was perturbed by the pattern in Figure 13b. The synthetic DCs of the perturbed model and corresponding to the observed paths were computed. We did not add any noise to the synthetic path-averaged DCs. We used the nonperturbed model as the initial model for the tomographic inversion.

In Figure 14a–14d, we show the recovered perturbations at different layers after the inversion. In the shallowest part of the model, the perturbations are better estimated (Figure 14a and 14b); however, the
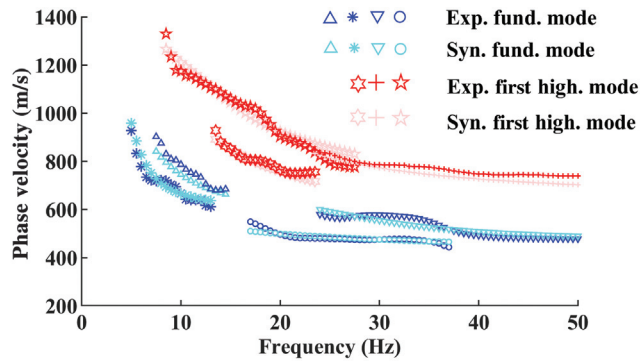

Figure 15. Examples of data fittings. Different markers represent different DCs, whereas the different colors separate the synthetic and experimental data, as well as the fundamental and first higher modes.
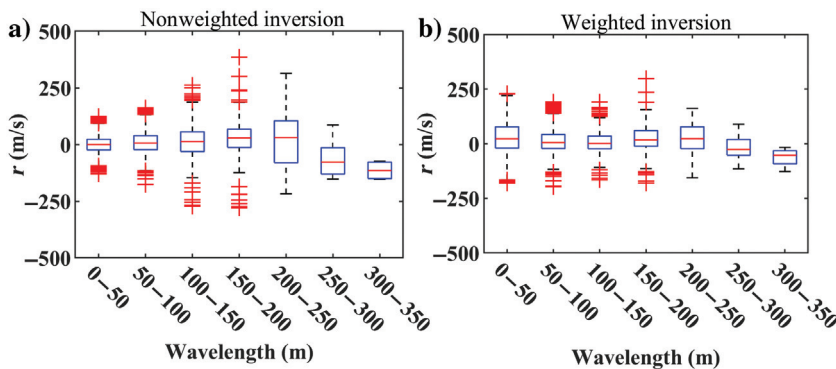

Figure 16. A box plot showing the residuals for different wavelength ranges. (a) Nonweighted inversion and (b) inversion with wavelength-based weights.

geometry of the perturbations (squares) is poorly recovered. This issue is mainly related to the data set's scale, the obtained data coverage (Figure 7b), and the nonuniform azimuthal illumination (Figure 7c).

DISCUSSION

We developed a method to automatically isolate the data to estimate different modes of surface waves and included the higher modes of surface waves in the SWT workflow. This approach is valid when the reference modes are separated in the frequency domain. In the case of surface wave mode superposition, the method can be applied to the high frequencies, where the separation of the modes is secured. For the data set, the computed first higher modes showed wavelength coverage up to 300 m (Figure 9f), whereas the fundamental mode's wavelength coverage was limited to 200 m. In addition, many of the higher modes' paths were unique with respect to the estimated fundamental modes. In Appendix B, using a synthetic example, we show the effect of including the higher modes on the inversion resolution.

The laterally constrained tomographic inversion well converged, and the synthetic DCs showed a proper fitting compared with the experimental ones. In Figure 15, we show examples of DC fittings at the last iteration of the inversion. Four fundamental modes and three first higher modes are displayed with distinct markers and colors.

We assigned weights to each data point based on the distribution of the wavelength. To better evaluate the impact of the weight on the DC fittings, we computed the residual misfit as

$$\mathbf{r} = \mathbf{vr}_{syn} - \mathbf{vr}_{obs}, \qquad (6)$$

where $\mathbf{vr}_{syn}$ and $\mathbf{vr}_{obs}$ are the vectors of synthetic (last iteration) and observed data points, respectively. In Figure 16a and 16b, we show a box plot of the residuals for the nonweighted and weighted SWT, respectively. The box plot is defined by three lines showing the 25th percentile, median, and 75th percentile of the residual's distribution and whisker lines extending from the box's edges up to 1.5 times the distance between the edges of the box. The rest of the data are considered outliers and represented by "+." We divided the residuals based on the wavelengths of the experimental data points to analyze the misfit within different ranges of wavelengths. For data points with wavelengths between 0 and 50 m, the nonweighted inversion (Figure 16a) shows slightly lower residuals compared to the weighted inversion (Figure 16b); however, for the rest of the data points with wavelengths larger than 50 m, the weighted inversion shows a considerably lower misfit. In addition, the significant underestimations of the synthetic DCs observed for the wavelengths greater than 250 m of the nonweighted inversion are well suppressed for the weighted inversion. The outliers in both cases are mainly from the paths close to the model's edges, with inadequate data coverage (Figure 10).

The azimuth distribution of the paths is an essential property of the data for tomographic inversion. A strongly nonuniform azimuthal distribution can drive the inversion to the direction of the dominant angles. The azimuthal illumination of the DC data (Figure 7c) showed a nonuniform distribution, with very few azimuthal angles between 25° and 130°. The checker-

board test confirmed the negative impact of paths' directionality: A limited portion and geometry of the perturbations were recovered (Figure 14). The directionality of the azimuths is mainly due to the limited number of available receivers and the source deployment's geometry. The latter could be overcome when more sparse locations of shots, covering multiple sides of the receivers, are available.

To show this, we performed another checkerboard test, adding 10 hypothetical source locations to the PNG acquisition geometry. In Figure 17, we show the 10 hypothetical source locations in green. We computed the additional synthetic path-averaged DCs using the model from the last iteration of the inversion and added them to the observed ones. We repeated the checkerboard test on the new data. In Figure 18, we show the checkerboard test results, in which the perturbations are better recovered compared with the checkerboard

test in Figure 14, in terms of the values and geometry of the perturbation.

CONCLUSION

We developed a multimodal SWT workflow that can be applied to challenging data sets acquired with irregular acquisition geometries. We use SWT to estimate the V_S model, and we use the skin depth of the surface-wave fundamental mode (the W/D method) to obtain the Poisson's ratio and transform the V_S model to the V_P model. We provided a method to automatically separate the multiple modes of the surface wave, avoiding the surface wave modal analysis for every receiver couple aligned with a source. The method's application to the data set confirms the possibility of obtaining near-surface V_S and V_P models from the data recorded in the framework of METIS. The resolution of the model is affected by the distribution of the azimuth angles. The checkerboard test that we performed on the hypothetical geometry of the acquisition confirms this observation and suggests a better expected resolution of the model if more diverse shot locations are used for the acquisition.

ACKNOWLEDGMENTS

DATA AND MATERIALS AVAILABILITY

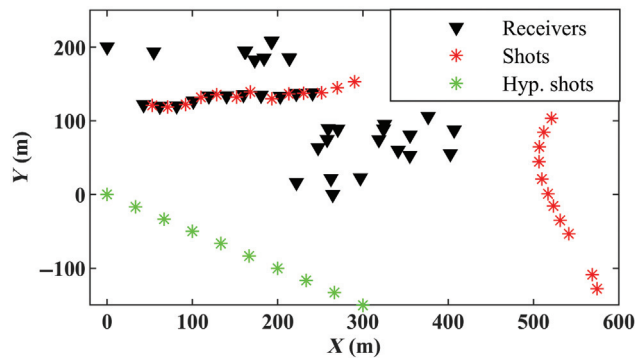Data associated with this research are confidential and cannot be released.

Figure 17. Hypothetical geometry of the PNG acquisition, in which 10 hypothetical sources' locations are added to the observed geometry in Figure 2a.

APPENDIX A

SYNTHETIC EXAMPLE: MULTIMODAL TWO-STATION PROCESSING METHOD

Here, we explain how the path-averaged DCs are estimated in the presence of two modes through the application of the two-station method to synthetic signals at two locations. We created the two signals containing two events at the expected times of the fundamental and the first higher modes of surface waves for the 1D layered system in Figure A-1a. The signals were obtained by convolving a Morlet wavelet with a time series containing a spike at the expected time for each mode and each frequency and then stacking on the whole frequency band (10–25 Hz). In Figure A-1a, we show the computed responses at positions 1000 m (T1) and 1200 m (T2). The processing workflow requires a velocity limit, which separates the fundamental and the first higher modes. For real data, we estimate the velocity limit from the multichannel analysis. Here, given the synthetic example, we obtained the velocity limit by averaging the phase velocities of the true fundamental and first higher
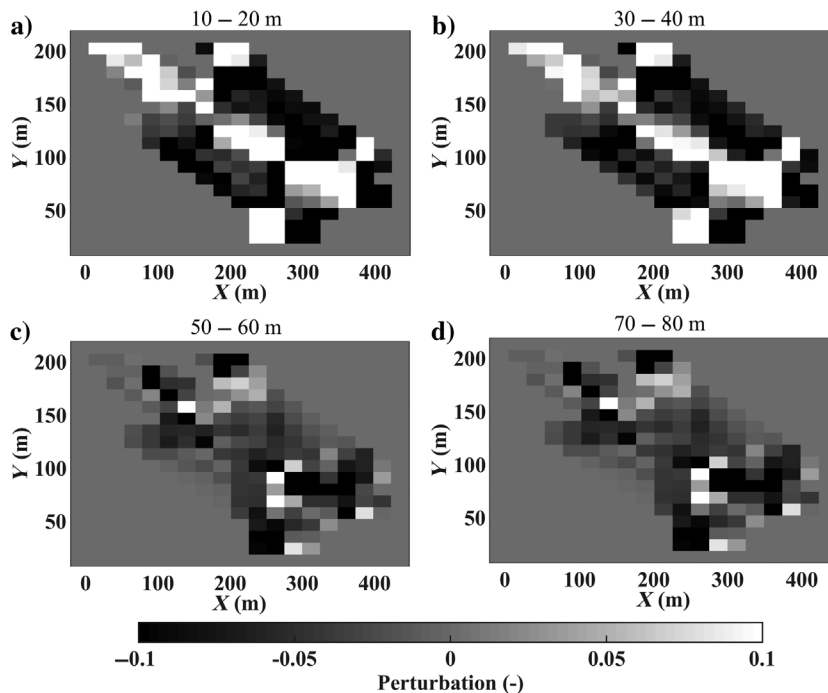

Figure 18. The checkerboard test performed to the hypothetical geometry of acquisition in Figure 17. The horizontal sections showing the layers at depths of (a) 10–20 m, (b) 30–40 m, (c) 50–60 m, and (d) 70–80 m.

modes at each frequency. In Figure A-1a, we also show the velocity limit in black; the blue and red hatches below and above the velocity limit are the fundamental and first higher mode zones, respectively. We apply the two-station method twice to estimate the fundamental and first higher modes of the surface waves.

In Figure A-1b and A-1c, we show, as examples, the processing steps applied to estimate the first higher mode at 10 Hz and the fundamental mode at 25 Hz, respectively. First, the velocity limit is transformed into time at the location of each trace (T1 and T2) by dividing the offsets (1000 m for T1 and 1200 m for T2)

to the velocity limit at the two considered frequencies (690 m/s at 10 Hz and 488 m/s at 25 Hz). Based on the arrival times (1.45 and 1.74 s for T1 and T2 at 10 Hz, and 2.05 and 2.46 s for T1 and T2 at 25 Hz), mutes are designed according to the intended mode estimation (the first panels of Figure A-1b for the first higher mode estimation at 10 Hz and Figure A-1c for the fundamental mode estimation at 25 Hz). The traces are multiplied (×) by the muting functions. Then, the muted traces are narrow-band filtered at the considered frequencies. We perform the filtering in the frequency domain by multiplying a narrow-banded zero-phase Gaussian filter centered at the desired frequencies (10 and 25 Hz) to the frequency domain representation of the traces (T1 muted and T2 muted). For a more straightforward representation of the filtering, in the second panels of Figure A-1b and A-1c, we show the filtering of T1 muted and T2 muted in the time domain as the convolution (*) to the 10 and 25 Hz filters. Finally, the muted and filtered traces are crosscorrelated (the third panels in Figure A-1b for the first higher mode at 10 Hz and Figure A-1c for the fundamental mode at 25 Hz). The processing method in Figure A-1b and A-1c shown at 10 and 25 Hz for the first higher and fundamental modes is repeated for all frequencies within the band 10–25 Hz. The crosscorrelated signals are assembled to form the crossmultiplication matrices in the first panels of Figure A-1d and A-1e. Knowing the distance between the two receivers (200 m), we use a third-order interpolator to transform the crossmultiplication matrix as a function of frequency and time delay to the same matrix as a function of frequency and velocity. In the second panel of Figure A-1d and A-1e, we show the estimated crossmultiplication matrices to estimate the fundamental and first higher modes, respectively; the trends of the true fundamental and first higher modes (the solid blue and solid red lines) are well obtained by the two matrices, except for the first higher mode above 23 Hz (the second panel in Figure A-1d).
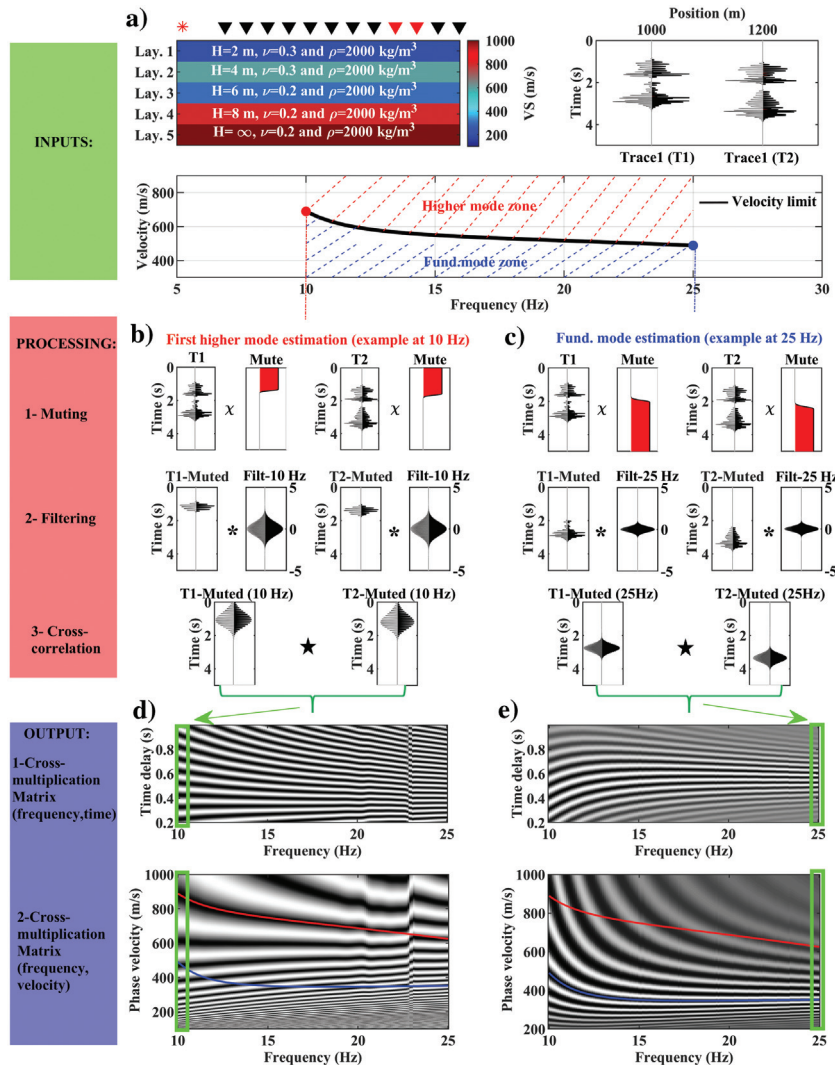

Figure A-1. The fundamental and first higher mode estimation of a synthetic example. (a) The inputs of the method: the mechanical properties of the laterally invariant example, the computed responses at location 1000 and 1200 m from the source, and the velocity limit separating the fundamental and the first higher mode zone. (b) The steps for phase velocity estimation of the first higher mode at 10 Hz. (c) The steps for the phase velocity estimation of the fundamental mode at 25 Hz. (d) The estimated cross-multiplication matrices in the frequency-time delay domain and the frequency-velocity domain aim to estimate the first higher mode. (e) The estimated cross-multiplication matrices in the frequency-time and the frequency-velocity domain aim to estimate the fundamental mode.
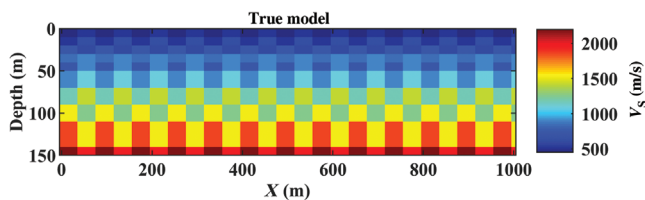

Figure B-1. The true synthetic model.

APPENDIX B

SYNTHETIC EXAMPLE: THE IMPACT OF HIGHER MODES AND WAVELENGTH-BASED WEIGHTS ON SWT

Here, we show the application of SWT to a synthetic 2D model to evaluate the effect of including the first higher mode as well as the
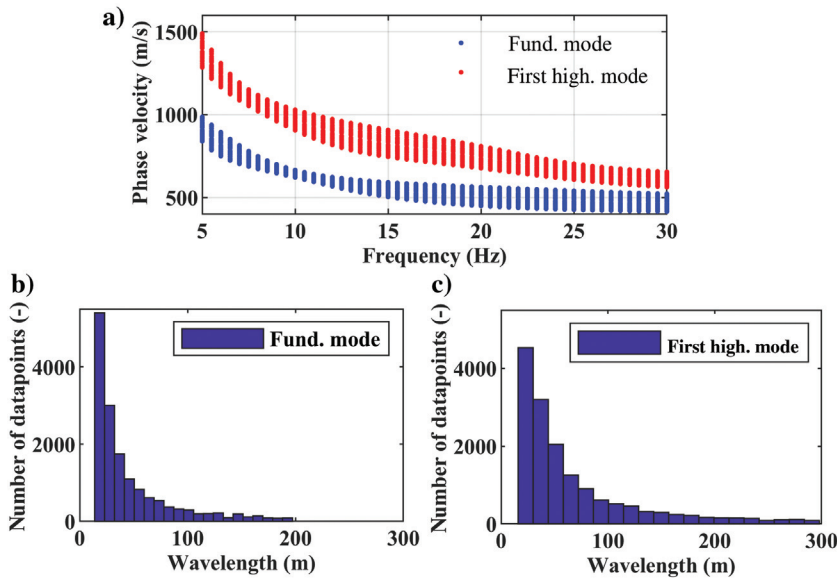
Figure B-2. (a) The computed fundamental and the first higher modes corresponding to the paths defined for the true model in Figure B-1. (b) The wavelength distribution of the fundamental mode data points. (c) The wavelength distribution of the first higher mode data points.
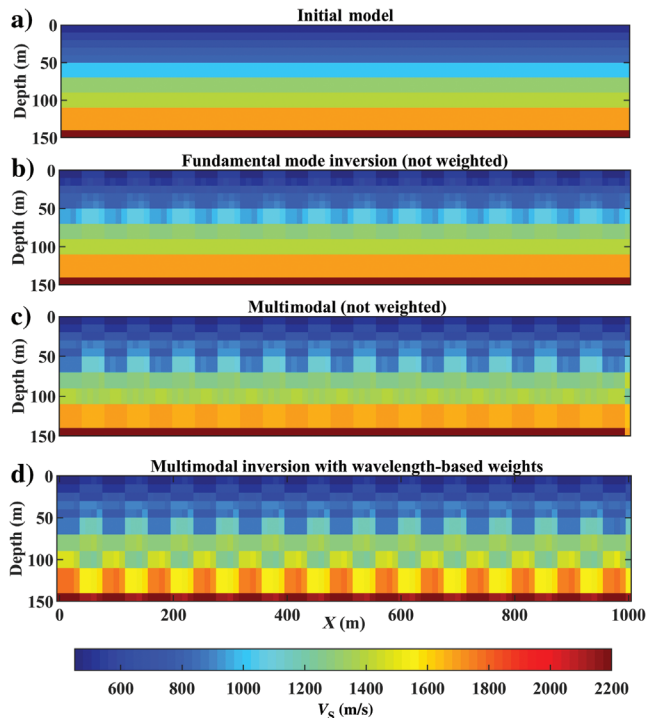

Figure B-3. The results of the tomographic inversion performed on the DCs of the synthetic example. (a) The initial model. (b) The estimated V_S model from the nonweighted fundamental mode inversion. (c) The estimated V_S model from the nonweighted multimodal inversion. (d) The estimated V_S model from weighted (wavelength-based) multimodal inversion.

impact of imposing the wavelength-based weights on the tomographic inversion. In Figure B-1, we show the true synthetic model, which consists of 101 1D models, evenly spaced. Along the 1 km line, we defined 612 paths with lengths ranging from 10 to 60 m. We computed the synthetic DCs corresponding to each path within the frequency range of 5–30 Hz. In Figure B-2a, we show the computed path-averaged surface wave fundamental and the first higher modes in blue and red, respectively.

In Figure B-2b and B-2c, we show the wavelength distribution corresponding to the data points of the fundamental and first higher modes, respectively. The wavelengths of the fundamental mode are limited to 200 m of wavelength, whereas the first higher mode has wavelength coverage up to 300 m of wavelength.

In Figure B-3a, we show the initial model used for the tomographic inversion. In Figure B-3b, we show the results of the inversion using only the fundamental mode and without imposing weights for the inversion. The results show a reasonable estimation of the first 70 m; however, the lateral and vertical variations are not fully recovered within the first 70 m of depth.

Then, we inverted the data using the fundamental mode and first higher modes, again without imposing weights to the data points (Figure B-3c). The inversion result shows much higher accuracy in recovering the first 70 m. In addition, the investigation depth is enhanced with respect to the fundamental mode inversion in Figure B-3b. In Figure B-3d, we show the result of the inversion using the fundamental mode and the first higher mode and by imposing wavelength-based weights, where it shows the successful recovery of the model up to 140 m in depth.

REFERENCES

Auken, E., and A. V. Christiansen, 2004, Layered and laterally constrained 2D inversion of resistivity data: Geophysics, **69**, 752–761, doi: 10.1190/1.1759461.

Badal, J., Y. Chen, M. Chourak, and J. Stankiewicz, 2013, S-wave velocity images of the Dead Sea Basin provided by ambient seismic noise: Journal of Asian Earth Sciences, **75**, 26–35, doi: 10.1016/j.jseaes.2013.06.017.

Bao, X., X. Song, and J. Li, 2015, High-resolution lithospheric structure beneath Mainland China from ambient noise and earthquake surface-wave tomography: Earth and Planetary Science Letters, **417**, 132–141, doi: 10.1016/j.epsl.2015.02.024.

Bergamo, P., and L. V. Socco, 2016, P- and S-wave velocity models of shallow dry sand formations from surface wave multi-modal inversion: Geophysics, **81**, no. 4, R197–R209, doi: 10.1190/geo2015-0542.1.

Boiero, D., 2009, Surface wave analysis for building shear wave velocity models: Ph.D. thesis, Politecnico di Torino.

Da Col, F., M. Papadopoulou, E. Koivisto, L. Sito, M. Savolainen, and L. V. Socco, 2019, Application of surface-wave tomography to mineral exploration: A case study from Siilinjärvi, Finland: Geophysical Prospecting, **68**, 254–269, doi: 10.1111/1365-2478.12903.

Ganji, V., N. Gucunski, and S. Nazarian, 1998, Automated inversion procedure for spectral analysis of surface waves: Journal of Geotechnical and Geoenvironmental Engineering, **124**, 757–770, doi: 10.1061/(ASCE)1090-0241(1998)124:8(757).

Halliday, D., and A. Curtis, 2008, Seismic interferometry, surface waves and source distribution: Geophysical Journal International, **175**, 1067–1087, doi: 10.1111/j.1365-246X.2008.03918.x.

Haskell, N., 1953, The dispersion of surface waves on multilayered media: Bulletin of the Seismological Society of America, **43**, 17–34, doi: 10.1029/SP030p0086.

Heisey, J. S., K. H. Stokoe, and A. H. Meyer, 1982, Moduli of pavement systems from spectral analysis of surface waves: Transportation Research Record, **852**, 22–31.

Khosro Anjom, F., and L. V. Socco, 2019, Improved surface wave tomography: Imposing wavelength-based weights: Gruppo Nazionale di Geofisica della Terra Solida (GNGTS).

Khosro Anjom, F., D. Teodor, C. Comina, R. Brossier, J. Virieux, and L. V. Socco, 2019, Full-waveform matching of VP and VS models from surface waves: Geophysical Journal International, **218**, 1873–1891, doi: 10.1093/gji/ggz279.

Lys, P. O., , the METIS team, Elder, K., and J. Archer, 2018, METIS, a disruptive R&D project to revolutionize land seismic acquisition: SEG Global Meeting, Expanded Abstracts, 28–31, doi: 10.1190/RDP2018-41752683.1.

Maraschini, M., 2008, A new approach for the inversion of Rayleigh and Scholte waves in site characterization: Ph.D. thesis, Politecnico di Torino.

Marquart, D., 1963, An algorithm for least squares estimation of nonlinear parameters: Journal of the Society of Industrial Applied Mathematics, **2**, 431–441.

Mi, B., J. Xia, C. Shen, L. Wang, Y. Hu, and F. Cheng, 2017, Horizontal resolution of multichannel analysis of surface waves: Geophysics, **82**, no. 3, EN51–EN66, doi: 10.1190/geo2016-0202.1.

Nazarian, S., H. Kenneth, K. H. Stokoe, and W. R. Hudson, 1983, Use of spectral analysis of surface waves method for determination of moduli and thicknesses of pavement systems: Transport Research Record, **930**, 38–45.

Pagliccia, B., K. Dalton, C. Walker, K. Elder, and R. Jenneskens, 2018, METIS hits the ground in Papua New Guinea, a field-proof innovative method to revolutionize onshore seismic acquisition: 80th Annual International Conference and Exhibition, EAGE, Extended Abstracts, B06, doi: 10.3997/2214-4609.201801402.

Park, C. B., R. D. Miller, and J. Xia, 1998, Imaging dispersion curves of surface waves on multi-channel record: 68th Annual International Meeting, SEG, Expanded Abstracts, 1377–1380, doi: 10.1190/1.1820161.

Picozzi, M., S. Parolai, D. Bindi, and A. Strollo, 2009, Characterization of shallow geology by high-frequency seismic noise tomography: Geophysical Journal International, **176**, 164–174, doi: 10.1111/j.1365-246X.2008.03966.x.

Shapiro, N. M., M. Campillo, L. Stehly, and M. H. Ritzwoller, 2005, High resolution surface wave tomography from ambient seismic noise: Science, **307**, 1615–1618, doi: 10.1126/science.1108339.

Socco, L. V., and D. Boiero, 2008, Improved Monte Carlo inversion of surface wave data: Geophysical Prospecting, **56**, 357–371, doi: 10.1111/j.1365-2478.2007.00678.x.

Socco, L. V., D. Boiero, P. Bergamo, F. Garofalo, H. Yao, R. D. Van der Hilst, and F. Da Col, 2014, Surface wave tomography to retrieve near surface velocity models: 84th Annual International Meeting, SEG, Expanded Abstracts, 2013–2018, doi: 10.1190/segam2014-1278.1.

Socco, L. V., and C. Comina, 2017, Time-average velocity estimation through surface-wave analysis — Part 2: P-wave velocity: Geophysics, **82**, no. 3, U61–U73, doi: 10.1190/geo2016-0368.1.

Socco, L. V., C. Comina, and F. Khosro Anjom, 2017, Time-average velocity estimation through surface-wave analysis — Part 1: S-wave velocity: Geophysics, **82**, no. 3, U49–U59, doi: 10.1190/geo2016-0367.1.

Socco, L. V., S. Foti, and D. Boiero, 2010, Surface wave analysis for building near surface velocity models: Established approaches and new perspectives: Geophysics, **75**, no. 5, 75A83–75A102, doi: 10.1190/1.3479491.

Thomson, W. T., 1950, Transmission of elastic waves through a stratified solid medium: Journal of Applied Geophysics, **21**, 89–93, doi: 10.1063/1.1699629.

Wespestad, C. E., C. H. Thurber, N. L. Andersen, B. S. Singer, C. Cardona, Z. Zeng, N. L. Bennington, K. Keranen, D. E. Peterson, D. Cordell, M. Unsworth, C. Miller, and G. W. Jones, 2019, Magma reservoir below Laguna del Maule Volcanic Field, Chile, imaged with surface-wave tomography: Journal of Geophysical Research, Solid Earth, **124**, 2858–2872, doi: 10.1029/2018JB016485.

Xia, J., R. D. Miller, C. B. Park, and G. Tian, 2003, Inversion of high frequency surface waves with fundamental and higher modes: Journal of Applied Geophysics, **52**, 45–57, doi: 10.1016/S0926-9851(02)00239-2.

Yao, H., R. D. Van der Hilst, and M. V. De Hoop, 2006, Surface-wave array tomography in SE Tibet from ambient seismic noise and two-station analysis — 1: Phase velocity maps: Geophysical Journal International, **166**, 732–744, doi: 10.1111/j.1365-246X.2006.03028.x.

Biographies and photographs of the authors are not available.